

RSC Advances



This is an *Accepted Manuscript*, which has been through the Royal Society of Chemistry peer review process and has been accepted for publication.

Accepted Manuscripts are published online shortly after acceptance, before technical editing, formatting and proof reading. Using this free service, authors can make their results available to the community, in citable form, before we publish the edited article. This *Accepted Manuscript* will be replaced by the edited, formatted and paginated article as soon as this is available.

You can find more information about *Accepted Manuscripts* in the [Information for Authors](#).

Please note that technical editing may introduce minor changes to the text and/or graphics, which may alter content. The journal's standard [Terms & Conditions](#) and the [Ethical guidelines](#) still apply. In no event shall the Royal Society of Chemistry be held responsible for any errors or omissions in this *Accepted Manuscript* or any consequences arising from the use of any information it contains.

A scalable formation of nano-SnO₂ anode derived from tin metal-organic frameworks for lithium-ion battery

Zixu Sun[†], Can Cao[‡], Wei-Qiang Han^{†,*}

[†]*Ningbo Institute of Materials Technology & Engineering, Chinese Academy of Sciences, Ningbo 315201, P. R. China*

[‡]*Department of Materials Science and Engineering, Zhejiang University, Hangzhou 310027, P. R. China*

*Correspondence and requests for materials should be addressed to W.Q.H. *e-mail:*

hanweiqiang@nimte.ac.cn

KEYWORDS: Sn-MOF, SnO₂, anode, flaky morphology, low-cost

ABSTRACT: In this work, for the first time, we synthesize a SnO₂ nanomaterial through the calcination of tin metal-organic framework (MOF) precursors. X-ray diffraction, field emission scanning electron microscope, transmission electron microscopy, and the Brunauer-Emmett-Teller specific surface area are used to characterize the phases and to observe surface morphologies. This anode material exhibits good electrochemical performance in LIBs with high reversible capacity and cycling stability. The good electrochemical properties could be ascribed to the short transport/diffusion path of electrons and lithium ions and the high contact area between the electrode and electrolyte that results from the nanostructured SnO₂. This is low-cost,

facile and scalable for mass production of SnO₂nanocomposites as a potential anode material for the next-generation LIBs.

1. Introduction

Rechargeable lithium-ion batteries (LIBs) are promising energy storage sources for many aspects of applications, such as portable electronic devices, electric vehicles, and stationary grid storage.^{1,2} New generation electrode materials with long cycle life, high capacity and high-rate performance are under extensive studies to meet the challenging requirements.^{1,2} Tin dioxide (SnO₂), one of the transition-metal oxides,³ is considered to be a promising candidate to substitute currently commercialized graphite anode for next generation LIBs owing to its high theoretical capacity of 782 mA h g⁻¹, appropriate working potential around 0.6 V (vs. Li⁺/Li), low cost, abundance, and environmental benignity.^{3,4} However, just like other transition-metal oxide electrodes, the practical applications of SnO₂-based anodes are still hindered by their poor cycling stability caused by the large volume change (240%) of SnO₂ during charge-discharge cycles, leading to the pulverization and electrical disconnection from the current collector.¹ One of attractive strategies to tackle these volume change-induced structural issues of SnO₂ is to decrease the size of the material because nanoparticles,⁵⁻⁸ compared to conventional bulk Sn is easily being oxidised on the surface.⁹⁻¹¹ It can alleviate the large strain of SnO₂ caused by lithium ion insertion/extraction, and can achieve excellent electrochemical performance due to the high contact area between active material and electrolyte.¹²⁻¹⁵

Metal-organic frameworks (MOFs) constructed by metal ions (clusters) and organic linkers are a new class of hybrid functional materials with large specific surface areas and high porosities, and have wide applications in catalysis, drug delivery, photochemical and electrochemical.¹⁶⁻²² Recently there have been many reports of using MOFs as precursors or

templates to synthesize nanoparticles and high specific surface area materials. There have also been many reports of the synthesis of metal oxide nanoparticles by direct calcination of MOFs, which exhibit excellent electrochemical performance.^{19-21, 23} Nevertheless, to the best of our knowledge, there has been no report on synthesis of SnO₂ nanoparticles with homogeneous morphology using MOFs as template. Herein we report a simple, scalable and low-cost synthesis of SnO₂ nanoparticles via the conversion of the Sn-MOF. When evaluated as an anode material for LIB, the as-prepared SnO₂ nanoparticles exhibit good electrochemical performance of a high reversible capacity and excellent stability of up to 100 charge/discharge cycles.

2. Experimental details

2.1 Reagents and Chemicals. Tin (II) sulfate (SnSO₄) and p-Phthalic acid (C₈H₆O₄) were purchased from Sinopharm Chemical Reagent Co. Ltd. Sodium hydroxide (NaOH, AR) was purchased from Aladdin Chemistry Co. Ltd. All chemicals were used as received without further purification.

2.2 Synthesis of Sn-MOF. In a typical procedure, 0.012 mol C₈H₆O₄ and 0.024 mol NaOH were dissolved in a 300 ml deionized water under stirring. After that, 60 mL of a 0.25 M SnSO₄ aqueous solution was simultaneously added dropwise into the above solution under constant stirring. The mixture was stirred for 5 h at room temperature until MOF precipitation was formed. The product was collected and washed with ethanol and deionized water for several times. At last, the white powder of Sn-MOF was dried in vacuum at 50 °C.

2.3 SnO₂ nanoparticles synthesis. The Sn-MOF was thermally treated at 400 °C for 2 h under air atmosphere with a ramping rate of 5 °C min⁻¹ and then naturally cooled down to room temperature. Finally, the product was taken out and it was found that the color of the material changed from white to gray.

2.4 Characterization. The composite was characterized by X-ray diffraction (XRD) which was carried out using an AXS D8 Advance Diffractometer (Cu-K α radiation, receiving slit 0.2mm, scintillation counter, 40mA, 40kV) in the range of $2\theta=10-90^\circ$. The microstructure and morphology of the as prepared composite were characterized using a Hitachi S-4800 field emission scanning electron microscope (SEM) and an FEI Tecnai G2 F20 transmission-electron microscopy (TEM) at an accelerating voltage of 200kV. The Brunauer-Emmett-Teller (BET) specific surface area was analyzed using N₂ absorption using an ASAP 2020M (Micromeritics Instrument Corp., USA).

2.5 Electrochemistry test. To evaluate the electrochemical performance, the electrodes were fabricated using the mixture made up of 80wt% active material, 10wt% acetylene black and 10wt% carboxymethyl cellulose (CMC). Lithium metal was used as the counter and reference electrode. The electrolyte was composed of a 1mol L⁻¹ LiPF₆ solution in fluoroethylene carbonate (FEC), dimethyl carbonate (DMC) and ethyl methyl carbonate (EMC) in 1:1:1(v/v/v) ratio. 2032 Coin cells were assembled in a glove box filled with high-purity argon. The charge-discharge measurement of the cells was conducted on a LAND CT2000 battery test system in a voltage range of 0.01-1.5V (versus Li⁺/Li). The cyclic voltammetry experiments were carried out on a CHI660 Electrochemical Workstation (Shanghai Chenhua) in the potential window from 0.01 to 1.5 V (vs. Li⁺/Li) at a scan rate of 0.05 mV s⁻¹. Electrochemical impedance spectroscopy (EIS) was carried out using a Solartron 1470E Electrochemical Interface (Solartron Analytical, UK) electrochemical workstation at 25 °C with the frequency ranging from 1 MHz to 0.01 Hz and AC signal of 10 mV in amplitude as the perturbation.

3. Results and discussion

The procedure of the preparation of SnO₂ nanoparticles was illustrated in **Fig. 1**. First, a simple synthesis of Sn-MOF composite with flaky morphology was developed. A subsequent thermal decomposition process was introduced to convert Sn-MOF into SnO₂ nanoparticles. The yield of SnO₂ from the Sn-MOF is about 46.8%. Field emission scanning electron microscopy (FESEM) was carried out to investigate the size and morphology of the products. As seen in **Fig. S1**, the as-prepared Sn-MOF composite was relatively uniform and appeared in flaky morphology with an average thickness of ~100 nm. **Fig. S2** showed X-ray diffraction (XRD) patterns of the prepared Sn-MOF composite.

The crystal structure of the samples was characterized by XRD. As shown in **Fig. 2**, the XRD patterns of the product could be readily indexed to the tetragonal phase SnO₂ (JCPDS no.:41-1445),²⁴ and no peaks from other impurities were observed, suggesting that the sample was of a pure phase.

N₂ adsorption-desorption measurement had been characterized on nano-SnO₂, as illustrated in **Fig. 3**. It was found that nano-SnO₂ had a Brunauer-Emmett-Teller (BET) specific surface area of 15.29 m² g⁻¹. The specific surface area of Sn-MOF was 14.24 m² g⁻¹. As seen in **Fig. 4**, the as-synthesized SnO₂ nanoparticles were relatively uniform and appear in spherical shape with an average diameter of around 40 nm, which is in good agreement with the result of the dynamic light scattering on SnO₂ nanoparticles (Fig. S4). The elemental composition of Sn-MOF was determined by the reaction equation. The result shown in Table S1 revealed that the as-prepared products contain Sn, C, O, and H, the mass percentages of them 41.98%, 33.95%, and 22.63%, and 1.44% respectively.

As shown in **Fig. 5a**, TEM characterization indicated that SnO₂ nanoparticles had a uniform size distribution with diameters between 30 and 50 nm, which was in good agreement with the

previous SEM observations in **Fig. 4**. The corresponding HR-TEM image (**Fig. 5b**) showed clear lattice fringes with a spacing of 0.34 nm, which corresponded to the (110) plane of the tetragonal phase.²⁵ The selected area electron diffraction (SAED) patterns comprised several bright concentric rings (**Fig. 5c**). The TEM image and the SADE of one small particle have been provided in Fig. S5. From Fig. S5, we can confirm that the SnO₂ particles are single crystalline. The elemental composition of nano-SnO₂ was determined by EDX analysis. The result displayed in Fig. 5d revealed that the as-prepared products contained Sn, O and Cu. Among these elements, Cu was generally influenced by the copper network support films.

The electrochemical properties of the nano-SnO₂ as an anode material for LIBs were evaluated. The active materials mass density loading in the electrode is about 0.6 mg cm⁻². **Fig. 6a** showed the charge/discharge profiles of the composite at a current density of 40 mA g⁻¹ between 0.01 and 1.5 V vs. Li⁺/Li. The first cycle discharge and charge capacities were 1600.9 and 832.4 mA h g⁻¹, respectively, corresponding to a high initial coulombic efficiency of 52.0%, which was remarkably higher than other reports.^{12, 26, 27} The capacity loss of the electrode in the first cycle could be mainly attributed to the irreversible reduction from SnO₂ to Sn and Li₂O and the formation of a solid electrolyte interphase (SEI) film. The charge/discharge capacities slightly increased in the subsequent cycles, which may be attributed to the activation of active materials. The reversible capacity of the nano-SnO₂ electrode is 850 mA h g⁻¹, much higher than the theoretical capacity of SnO₂,^{9, 22, 23} which might be attributed to the partially reversible reaction of Li₂O and Sn to SnO₂.^{28, 29} **Fig. 6b** displayed the cyclic voltammogram (CV) profiles of the nano-SnO₂ electrode in a potential window of 0.01-1.5V (vs. Li⁺/Li) at a scanning rate of 0.05 mVs⁻¹ for the first 8 cycles. In the first half-cycle, three broad cathodic peaks at around 1.25, 0.85 and 0.24 V could be ascribed to the decomposition of SnO₂ to Sn and Li₂O, the

formation of a SEI film, which disappeared under the subsequent cycles,³⁰ and finally the alloying reaction between Sn and Li⁺, respectively. In the case of the first anodic process, two broader anodic peaks at 0.48 and 0.60 V corresponded to the extraction of lithium ion from Li-Sn alloys. Note that another oxidation peak at 1.25 V was also observed, which was most likely due to the partially reversible reaction of SnO₂ to Sn and Li₂O.³¹ CV behavior presented remarkably repeatable shapes after the first cycle demonstrating high reversibility of the charge/discharge process.

The cycle performance together with the coulombic efficiency of the nano-SnO₂ material at a current density of 400 mA g⁻¹ were shown in **Fig. 7a**. The initial coulombic efficiency relatively low was 52.0%, and then after a few charge-discharge cycles, the nano-SnO₂ material exhibited good capacity retention and their coulombic efficiency steadily remains higher than 99%, which was mainly attributed to the unique feature of the nanostructured SnO₂. Nanostructures can alleviate the large strain of Sn during alloying/dealloying process and can effectively decrease the transport/diffusion path of electrons and lithium ions. For the first three cycles, the electrode was activated at a higher current density of 40 mA g⁻¹, and for the following cycles, it was 400 mA g⁻¹. At the end of 100 cycles, a reversible capacity of ~541.8 mA h g⁻¹ could still be retained. The cycling performance for Sn-MOF material has been provided in Fig. S6. The capacity of the Sn-MOF material is only 198 mA h g⁻¹ at a current density of 400 mA g⁻¹ after 50 cycles, which shows a lower capacity than the SnO₂. The rate capability of the electrode was evaluated at different current densities from 40 mA g⁻¹ to 3.2 A g⁻¹, as shown in **Fig. 7b**. The anode material exhibited rate capability with capacities of 400 mA h g⁻¹ at 1.6 A g⁻¹ and 285 mA h g⁻¹ at 3.2 A g⁻¹, which demonstrated that the nano-SnO₂ anode had good rate capability and high coulombic

efficiency. From these results, it is believed that the excellent rate performance of the nano-SnO₂ anode is associated with the relatively small particle size and large surface area.

The EIS of the nano-SnO₂ electrode was investigated to gain further insights into the superior rate capability and the stable cycling performance (**Fig. 8**). The frequency range was set between 1MHz and 0.01Hz, and EIS was carried out on the sample after being charged to 1.5 V at 40mA g⁻¹ in the 1th, 2th, 5th and 50th cycle, respectively. The Nyquist plots showed a depressed semicircle at high frequency and a straight line at low frequency. The diameter of the depressed semicircle represented the resistance of the charge-transfer process, while the straight line corresponded to the diffusion of lithium ion in the nano-SnO₂ electrode. The Randles equivalent electrical circuit and the values of R_{ct} for the nano-SnO₂ electrode were shown in Fig. S7 and Table S2. It could be seen that there was even a slight decrease in charge-transfer resistance after 50 charge-discharge cycles, demonstrating that the nano-SnO₂ electrode having a stabilized state and the good reaction kinetics in the charge-discharge process, which was consistent with the good cycling stability of the composite.

3. Conclusions

In summary, for the first time, we synthesized a nano-SnO₂ material through the calcination of MOF precursors, which involved the preparation of the Sn-MOF template and subsequent thermal decomposition of the template in an air atmosphere at the temperature of 400 °C. The as-prepared nano-SnO₂ exhibited good electrochemical performance in LIBs with high reversible capacity and excellent cycling stability and good rate capability. The good electrochemical properties could be ascribed to the short transport/diffusion path of electrons and lithium ions and the high contact area between the electrode and electrolyte that result from the nanostructured SnO₂. The synthetic route was low-cost, facile and scalable for mass production

of the SnO₂ as a potential anode material for the next-generation LIBs with improved energy density capacity.

Acknowledgements

This work was financially supported by the “Strategic Priority Research Program” of the Chinese Project Academy of Science (Grant no. XDA09010201), the National Natural Science Foundation of China (Grant no. 51371186), Ningbo 3315 International Team of Advanced Energy Storage Materials, Zhejiang Province Key Science and Technology Innovation Team (Grant no. 2013TD16).

Reference

1. M. V. Reddy, G. V. Subba Rao and B. V. R. Chowdari, *Chemical Reviews*, 2013, 113, 5364-5457.
2. M. N. Obrovac and V. L. Chevrier, *Chemical reviews*, 2014, 114, 11444-11502.
3. Z. Chen, D. Pan, Z. Li, Z. Jiao, M. Wu, C.-H. Shek, C. M. L. Wu and J. K. L. Lai, *Chemical Reviews*, 2014, 114, 7442-7486.
4. X. Zhou, L.-J. Wan and Y.-G. Guo, *Advanced materials*, 2013, 25, 2152-2157.
5. M.-S. Park, Y.-M. Kang, G.-X. Wang, S.-X. Dou and H.-K. Liu, *Advanced Functional Materials*, 2008, 18, 455-461.
6. S. Chen, Y. Xin, Y. Zhou, F. Zhang, Y. Ma, H. Zhou and L. Qi, *Journal of Materials Chemistry A*, 2014, 2, 15582.
7. B. P. Vinayan and S. Ramaprabhu, *Journal of Materials Chemistry A*, 2013, 1, 3865.
8. X. Fan, J. Shao, X. Xiao, X. Wang, S. Li, H. Ge, L. Chen and C. Wang, *J. Mater. Chem. A*, 2014, 2, 18367-18374.
9. X. L. Wang, M. Feyngenson, H. Chen, C. H. Lin, W. Ku, J. Bai, M. C. Aronson, T. A.

- Tyson and W. Q. Han, *Journal of the American Chemical Society*, 2011, 133, 11213-11219.
10. X. L. Wang, W. Q. Han, J. Chen and J. Graetz, *ACS applied materials & interfaces*, 2010, 2, 1548-1551.
 11. F. Xin, X. Wang, J. Bai, W. Wen, H. Tian, C. Wang and W. Han, *Journal of Materials Chemistry A*, 2015, 3, 7170-7178.
 12. Y. Yan, F. Du, X. Shen, Z. Ji, X. Sheng, H. Zhou and G. Zhu, *J. Mater. Chem. A*, 2014, 2, 15875-15882.
 13. C. Hou, X.-M. Shi, C.-X. Zhao, X.-Y. Lang, L.-L. Zhao, Z. Wen, Y.-F. Zhu, M. Zhao, J.-C. Li and Q. Jiang, *Journal of Materials Chemistry A*, 2014, 2, 15519.
 14. R. Liu, S. Yang, F. Wang, X. Lu, Z. Yang and B. Ding, *ACS applied materials & interfaces*, 2012, 4, 1537-1542.
 15. Y. Chen, J. Lu, S. Wen, L. Lu and J. Xue, *J. Mater. Chem. A*, 2014, 2, 17857-17866.
 16. R. R. Salunkhe, Y. Kamachi, N. L. Torad, S. M. Hwang, Z. Sun, S. X. Dou, J. H. Kim and Y. Yamauchi, *J. Mater. Chem. A*, 2014, 2, 19848-19854.
 17. J.-K. Sun and Q. Xu, *Energy & Environmental Science*, 2014, 7, 2071.
 18. A. Morozan and F. Jaouen, *Energy & Environmental Science*, 2012, 5, 9269.
 19. R. Wu, X. Qian, F. Yu, H. Liu, K. Zhou, J. Wei and Y. Huang, *Journal of Materials Chemistry A*, 2013, 1, 11126.
 20. Y. Lü, W. Zhan, Y. He, Y. Wang, X. Kong, Q. Kuang, Z. Xie and L. Zheng, *ACS applied materials & interfaces*, 2014, 6, 4186-4195.
 21. X. Xu, R. Cao, S. Jeong and J. Cho, *Nano letters*, 2012, 12, 4988-4991.
 22. L. He, L. Li, L. Zhang, S. Xing, T. Wang, G. Li, X. Wu, Z. Su and C. Wang,

- CrystEngComm*, 2014, 16, 6534.
23. K. Shiva, K. Jayaramulu, H. B. Rajendra, T. Kumar Maji and A. J. Bhattacharyya, *Zeitschrift für anorganische und allgemeine Chemie*, 2014, 640, 1115-1118.
 24. S.-K. Park, S.-H. Yu, N. Pinna, S. Woo, B. Jang, Y.-H. Chung, Y.-H. Cho, Y.-E. Sung and Y. Piao, *Journal of Materials Chemistry*, 2012, 22, 2520.
 25. N. Liu, Z. Lu, J. Zhao, M. T. McDowell, H. W. Lee, W. Zhao and Y. Cui, *Nature nanotechnology*, 2014, 9, 187-192.
 26. Z. Yang, Q. Meng, Z. Guo, X. Yu, T. Guo and R. Zeng, *Journal of Materials Chemistry A*, 2013, 1, 10395.
 27. A. Bhaskar, M. Deepa and T. N. Rao, *Nanoscale*, 2014, 6, 10762.
 28. W. Zhou, J. Wang, F. Zhang, S. Liu, J. Wang, D. Yin and L. Wang, *Chemical communications*, 2015, 51, 3660-3662.
 29. C. Gong, Y. Zhang, M. Yao, Y. Wei, Q. Li, B. Liu, R. Liu, Z. Yao, T. Cui, B. Zou and B. Liu, *RSC Adv.*, 2015, 5, 39746-39751.
 30. X. Zhang, R.-S. Kuhnel, M. Schroeder and A. Balducci, *Journal of Materials Chemistry A*, 2014, 2, 17906-17913.
 31. B. Zhou, S. Yang, L. Wu, W. Wu, W. Wei, L. Chen, H. Zhang, J. Pan and X. Xiong, *RSC Adv.*, 2015, 5, 49926-49932.

Figure Captions

Fig. 1 Schematic illustration of the formation of SnO₂ nanoparticles.

Fig. 2 XRD patterns of the as-synthesized nano-SnO₂.

Fig. 3 N₂ adsorption-desorption measurement of the nano-SnO₂.

Fig. 4 (a) Low- and (b) high-magnified FESEM images of products obtained after heating Sn-MOF at 400 °C.

Fig. 5 TEM image of the obtained nano-SnO₂ (a), High-resolution TEM image (b), selected area Electron Diffraction (SAED) Spectroscopy (c) and EDX profile (d).

Fig. 6 (a) Galvanostatic charge/discharge profiles of the nano-SnO₂ anode at a current density of 40 mA g⁻¹. (b) Cyclic voltammogram of the 1st to 8th cycle of the as-prepared nano-SnO₂ composite between 0.01 to 1.5 V (vs. Li⁺/Li) at a scanning rate of 0.05 mV s⁻¹.

Fig. 7 (a) Cycling performance of the nano-SnO₂ electrode at a current density of 400 mA g⁻¹. (b) Rate capability of nano-SnO₂ at different discharge currents.

Fig. 8 Nyquist plots of the electrodes of the nano-SnO₂ composite after 1, 2 and 5 charge-discharge cycles at 40 mA g⁻¹, obtained after charging to 1.5 V.

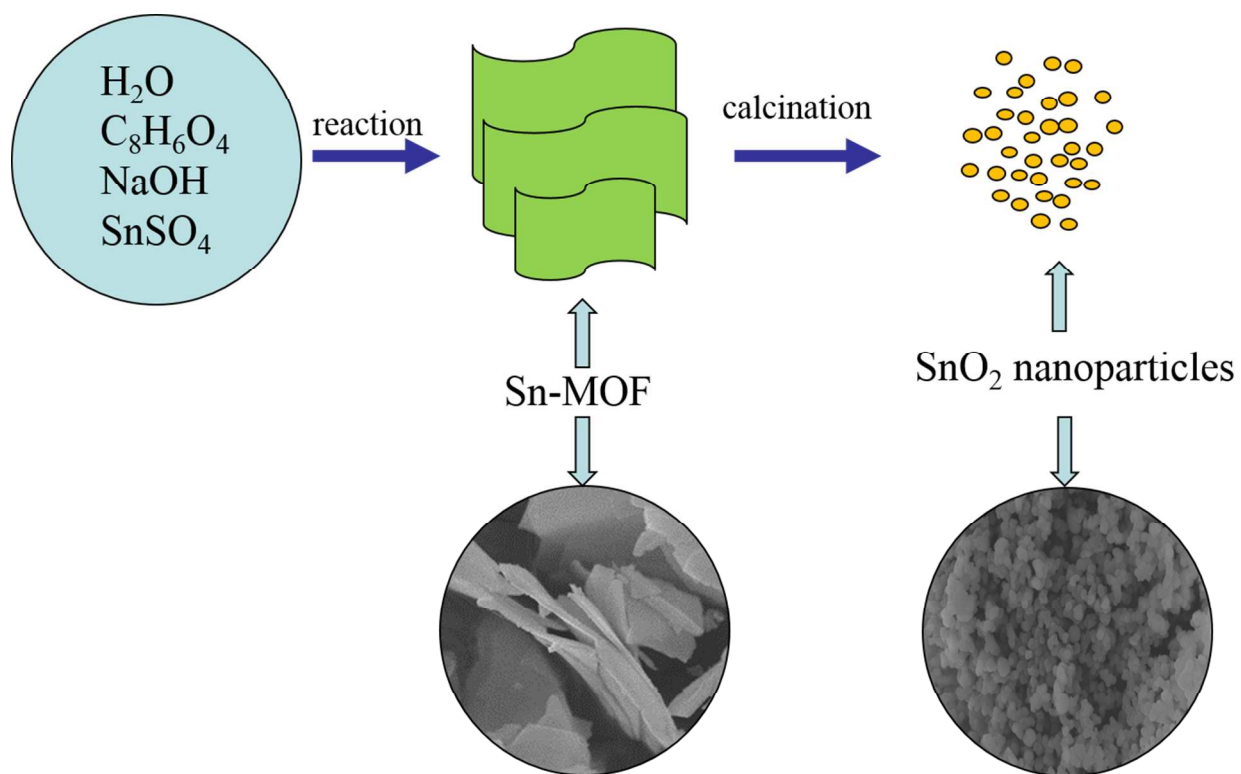


Fig. 1 Schematic illustration of the formation of SnO₂ nanoparticles.

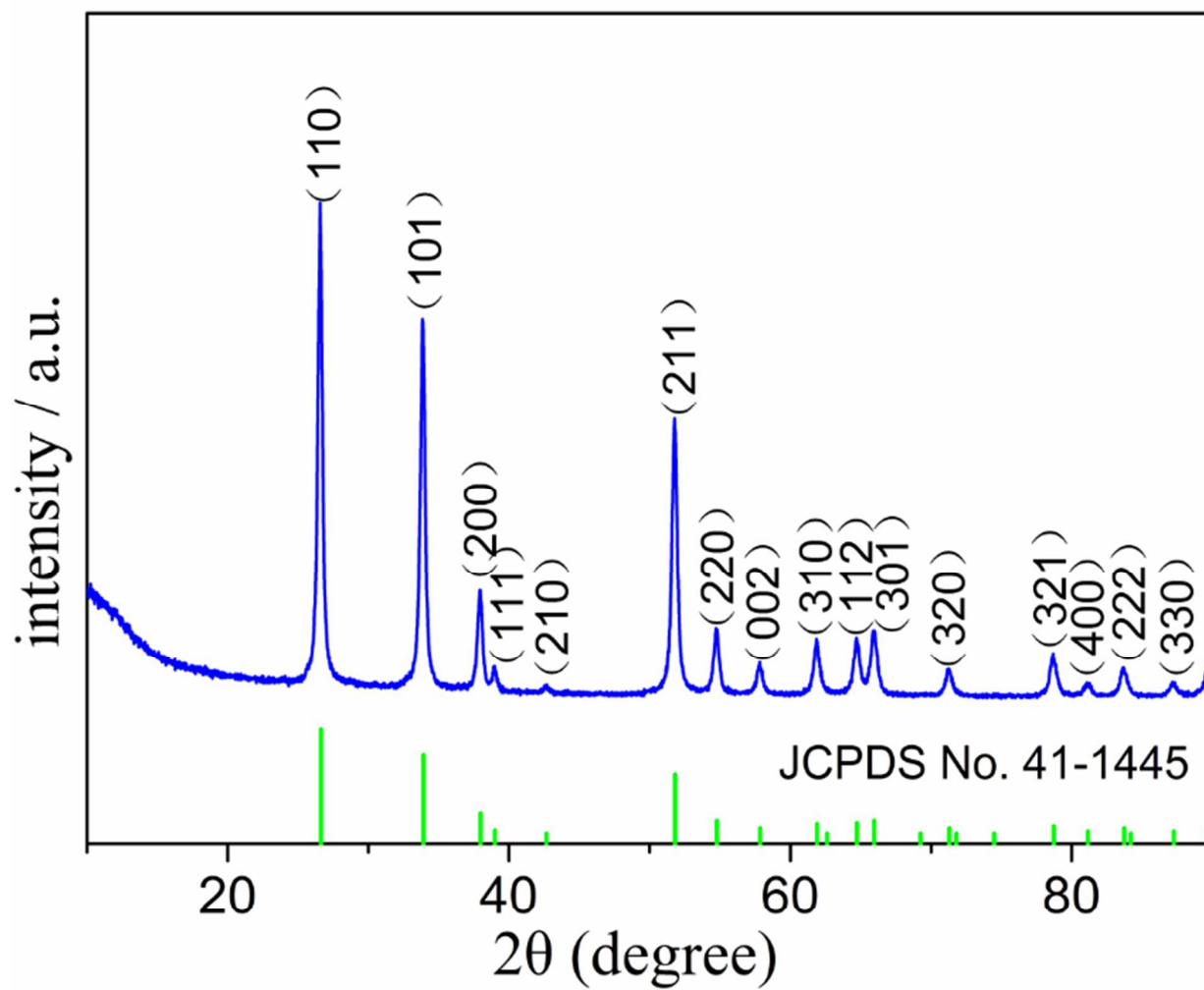


Fig. 2 XRD patterns of the as-synthesized nano-SnO₂.

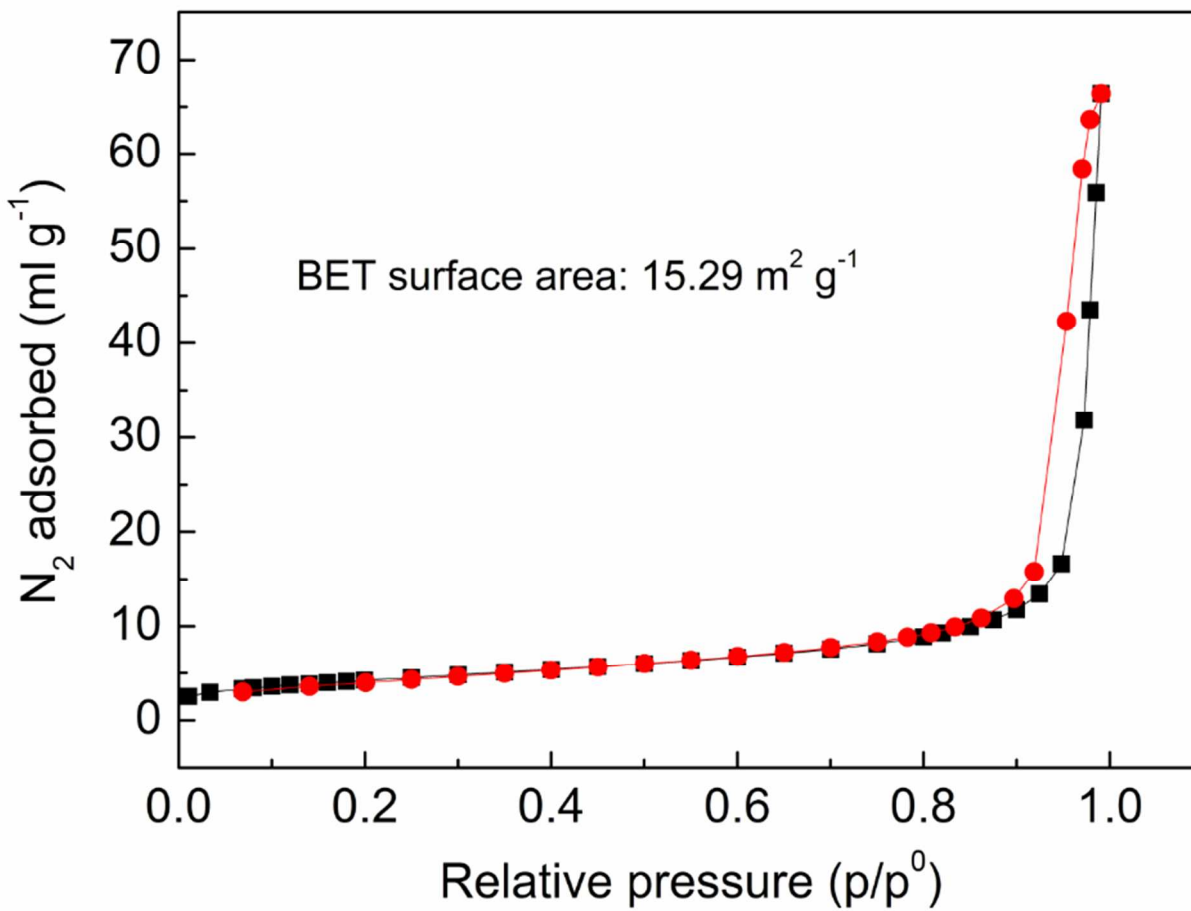


Fig. 3 N₂ adsorption-desorption measurement of the nano-SnO₂.

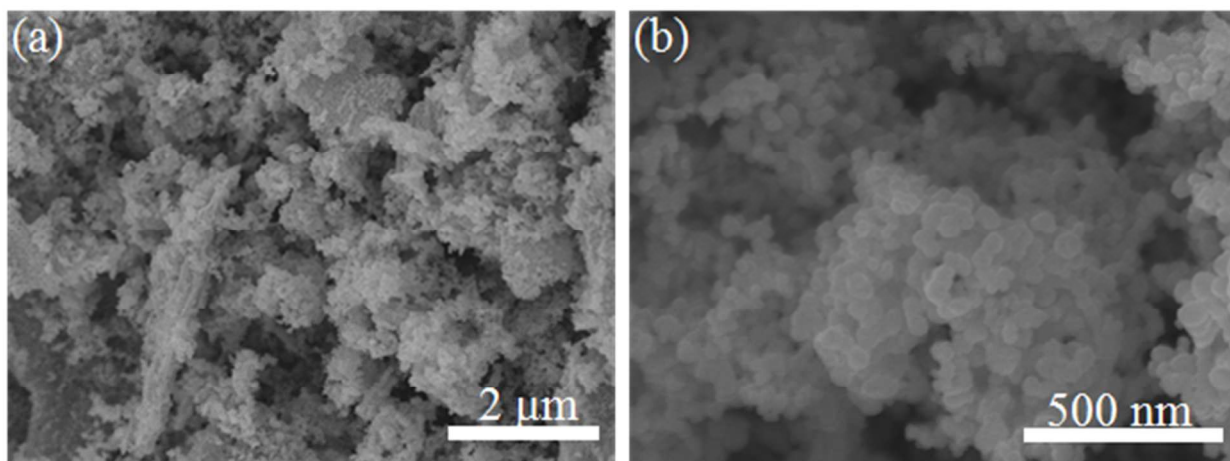


Fig. 4 (a) Low- and (b) high-magnified FESEM images of products obtained after heating Sn-MOF at 400 °C.

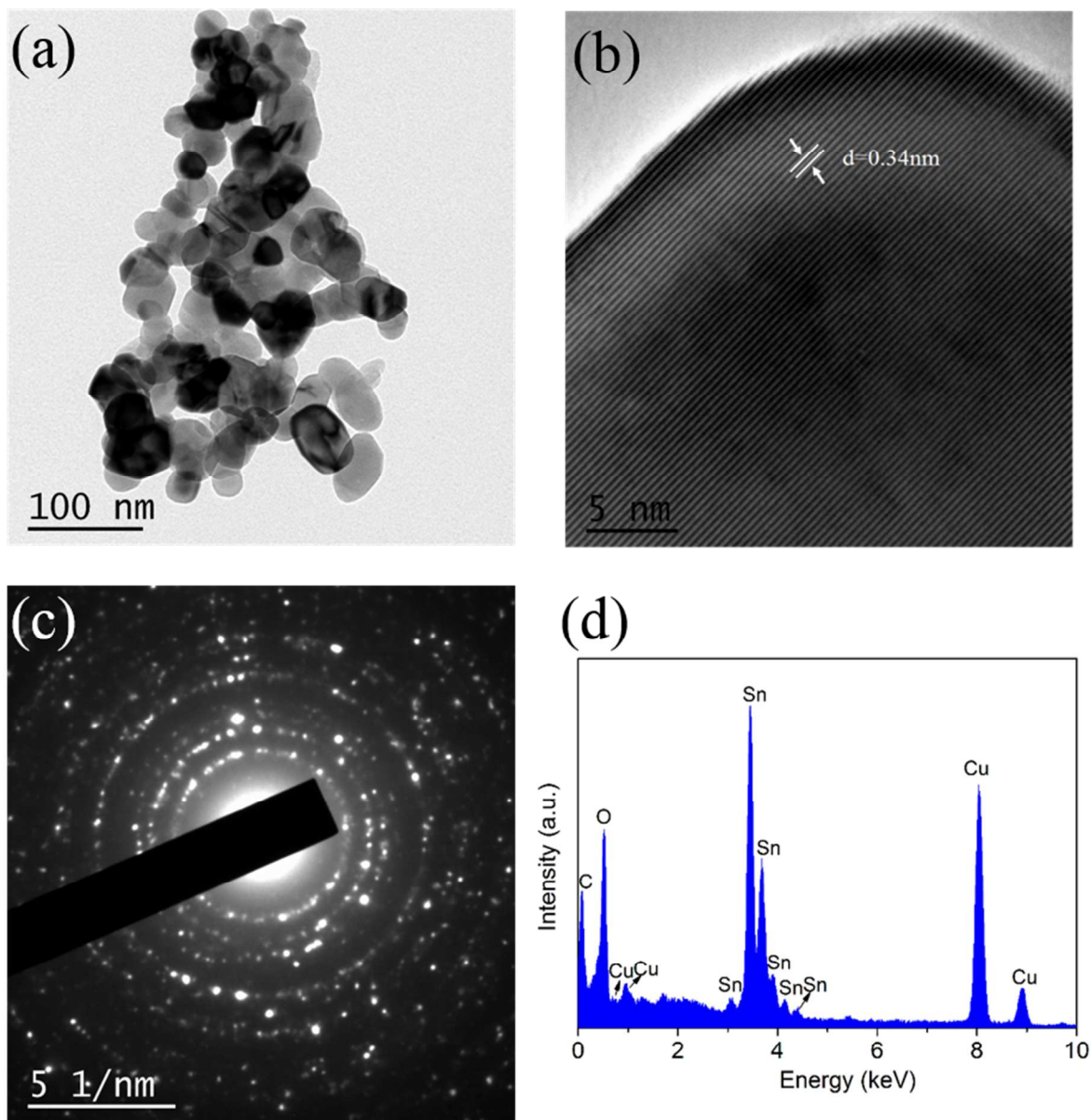


Fig. 5 TEM image of the obtained nano-SnO₂ (a), High-resolution TEM image (b), selected area Electron Diffraction (SAED) Spectroscopy (c) and EDX profile (d).

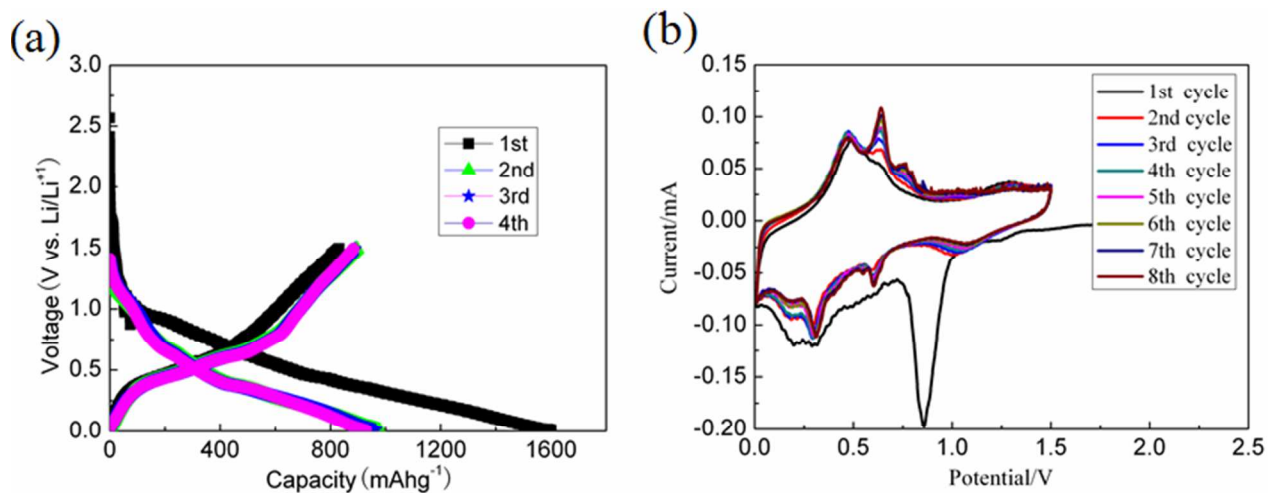


Fig. 6 (a) Galvanostatic charge/discharge profiles of the nano-SnO₂ anode at a current density of 40 mA g⁻¹. (b) Cyclic voltammogram of the 1st to 8th cycle of the as-prepared nano-SnO₂ composite between 0.01 to 1.5 V (vs. Li⁺/Li) at a scanning rate of 0.05 mV s⁻¹.

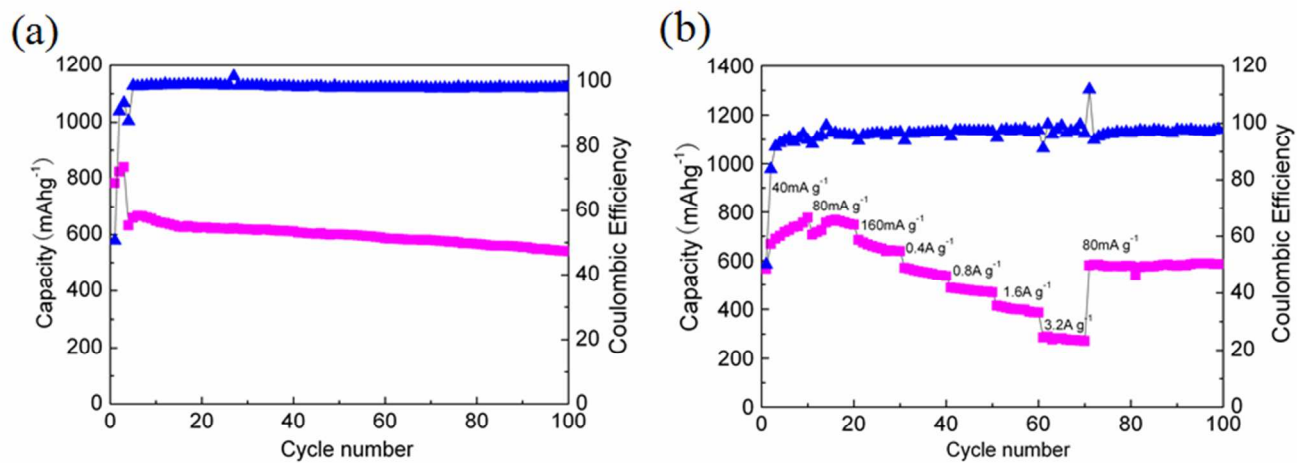


Fig. 7 (a) Cycling performance of the nano-SnO₂ electrode at a current density of 400 mA g⁻¹.

(b) Rate capability of nano-SnO₂ at different discharge currents.

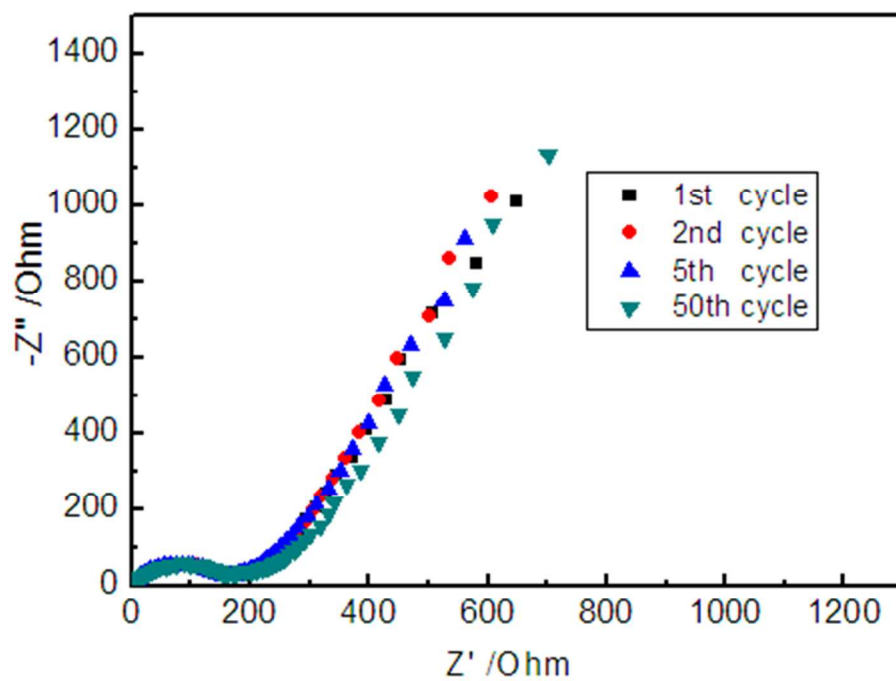


Fig. 8 Nyquist plots of the electrodes of the nano-SnO₂ composite after 1, 2 and 5 charge-discharge cycles at 40 mA g⁻¹, obtained after charging to 1.5 V.

Graphical Abstract

